ACS APPLIED MATERIALS & INTERFACES

Research Article

www.acsami.org

Synthesis of NiO Nanofibers Composed of Hollow Nanospheres with Controlled Sizes by the Nanoscale Kirkendall Diffusion Process and Their Electrochemical Properties

Jung Sang Cho, Seung Yeon Lee, Hyeon Seok Ju, and Yun Chan Kang*

Department of Materials Science and Engineering, Korea University, Anam-Dong, Seongbuk-Gu, Seoul 136-713, Republic of Korea

Supporting Information

ABSTRACT: NiO nanofibers composed of hollow NiO nanospheres with different sizes were prepared by electrospinning method. The mean size of the hollow NiO nanospheres was determined by the mean size of the Ni nanocrystals of the Ni−C composite nanofibers formed as an intermediate product. Porous-structured NiO nanofibers were also prepared as a comparison sample by direct oxidation of the electrospun nanofibers. The discharge capacities of the nanofibers composed of hollow nanospheres reduced at 300, 500, and 700 °C for the 250th cycle were 707, 655, and 261 mA h g^{-1}, respectively. However, the discharge capacity of the porous-structured NiO nanofibers for the 250th cycle was low as 206 mA h g^{-1}. The nanofibers composed of hollow nanospheres had good structural stability during cycling.

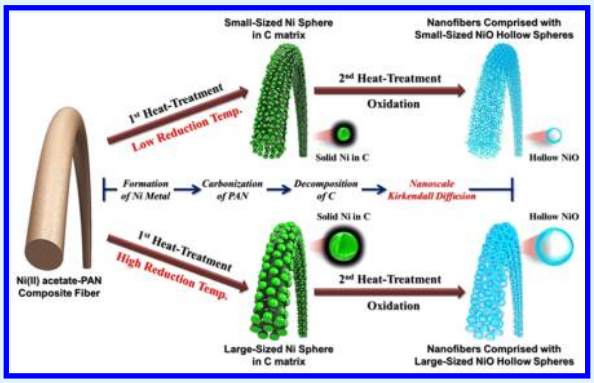

KEYWORDS: *Kirkendall diffusion, hollow nanopowders, nickel oxide, lithium-ion batteries, electrospinning*

INTRODUCTION

Transition metal oxides with high capacities have been widely investigated as alternative anode materials for lithium-ion batteries (LIBs).[1−6] Hollow spheres have been intensively studied as anode materials owing to their many advantages.[7−18] Wang et al. synthesized hollow Co_3O_4 nanoparticles via an impregnation reduction method followed by air oxidation.[16] The hollow Co_3O_4 exhibited excellent discharge capacity and durable performance compared to nonhollow structures. Li et al. synthesized SnO_2 hollow nanopowders by calcining SnO_2-coated PS nanospheres.[17] The SnO_2 hollow nanopowders exhibited good electrochemical properties for lithium-ion storage. Additionally, Lou et al. prepared α-Fe_2O_3 hollow nanospheres via a glycerol/water quasi-emulsion-templating mechanism.[18] The hollow α-Fe_2O_3 spheres exhibited significantly improved Li storage capabilities.

Efforts have also been carried out to build one-dimensionally (1D) structured metal oxides as anode materials.[19−24] These 1D geometries allow efficient electron transport and decrease of lithium-ion diffusion length. Therefore, the application of 1D geometries to the hollow nanostructure has been considered attractive for use in LIBs, and various synthetic methods are being explored.[25−31] For example, Chaudhari and Srinivasan synthesized hollow-structured α-Fe_2O_3 nanofibers by a simple electrospinning technique and subsequent calcination process.[25] Wang et al. synthesized hierarchical NiO microtubes by calcination of nickel dimethylglyoxime microtubes.[26] Han et al. synthesized hollow nitridated TiO_2 nanofibers using a electrospinning method.[27]

NiO, with its outstanding theoretical capacity (~718 mA h g^{-1}), chemical and thermal stability, and high abundance, has been regarded as a particularly promising candidate for anodes.[26,31−36] Various types of nanostructured NiO materials have been studied to achieve the good electrochemical properties for lithium-ion storage. Despite these efforts, the energy density, rate capability, and cycle stability of NiO remain unsatisfactory among the transitional metal oxides. Here, we suggest a novel 1D nanostructure composed of hollow NiO nanospheres as high power anode materials to satisfy the electrochemical requirements in LIBs. In this study, the electrochemical properties of nanofibers composed of hollow NiO nanospheres were compared with those of porous-structured NiO nanofibers, as anode materials for LIBs. In addition, the effect of the heat-treatment temperature on the formation mechanism of the NiO nanofibers was investigated in detail from the viewpoint of the Kirkendall diffusion effect.

EXPERIMENTAL SECTION

Nickel(II) acetate tetrahydrate−polyacrylonitrile ($Ni(OCOCH_3)_2 \cdot 4H_2O$−PAN) nanofibers were synthesized by an electrospinning method as described in our previous literature.[28,29] The solution was prepared by dissolving 6 g of $Ni(OCOCH_3)_2 \cdot 4H_2O$ and 4 g of PAN (M_w, 150,000) in a solution of 50 mL of *N*,*N*-dimethylformamide (DMF) with vigorous stirring overnight. The reduction processes of the electrospun nanofibers were conducted at 300, 500, and 700 °C for

Received: June 21, 2015
Accepted: November 9, 2015
Published: November 9, 2015

DOI: 10.1021/acsami.5b08793
ACS Appl. Mater. Interfaces 2015, 7, 25641−25647

5 h under 10% H_2/Ar mixture gas. The subsequent oxidation process was conducted at 400 °C for 5 h in air. For simplicity, the NiO nanofibers composed of hollow nanospheres formed by reduction at 300, 500, and 700 °C in 10% H_2/Ar, and subsequent oxidation at 400 °C in air, are referred to as "Kirkendall-300", "Kirkendall-500", and "Kirkendall-700" nanofibers, respectively. The one-step posttreatment of the electrospun nanofibers at 500 °C for 5 h under an air atmosphere produced the porous-structured NiO nanofibers as a comparison sample.

The electrochemical properties of the nanofibers were analyzed by constructing a 2032-type coin cell as described in our previous literature.[28,29] The discharge/charge characteristics of the nanofibers were investigated by cycling within the 0.001−3 V potential range.

RESULTS AND DISCUSSION

The characteristics of the electrospun nanofibers are shown in Supporting Information (SI) Figure S1. After stabilization at 250 °C for 1 h, the electrospun nanofibers are stable during posttreatment such that melting of the nanofibers and necking between the nanofibers do not occur. The stabilized $Ni(OCOCH_3)_2{\cdot}4H_2O$−PAN nanofibers shown in SI Figure S1a have a mean diameter of 350 nm. TGA of the electrospun nanofibers (SI Figure S1b) shows complete decomposition of nickel acetate and the PAN polymer at temperatures below 350 °C. Supporting Information Figure S2 shows the crystal structures of the electrospun nanofibers reduced at 300, 500, and 700 °C. The XRD patterns show complete conversion of nickel acetate into metallic Ni, irrespective of the reduction temperature. The morphologies of the Ni−C nanofibers formed at a reduction temperature of 500 °C are shown in Figure 1. The overall morphology of the nanofibers is maintained even after the reduction process. However, the solid structure of the electrospun nanofibers transforms into the porous structure after reduction. The formation of Ni nanocrystals during the reduction process, by decomposition and reduction of nickel acetate and carbonization of PAN, results in porous Ni−C nanofibers. The TEM images in Figure 1c clearly show the Ni nanocrystals dispersed within the carbon matrix. The high-resolution TEM image in Figure 1d reveals the formation of graphitic carbon during the reduction process, for which metallic Ni nanocrystals act as a catalyst. Figure 1e clearly reveals the lattice fringes separated by 0.2 nm, which corresponds to the (111) crystal plane of Ni metal. The selected area electron diffraction (SAED) pattern in Figure 1f also reveals the crystalline structure of the Ni metal. The elemental mapping images in Figure 1g show that the Ni component is uniformly distributed throughout the carbon matrix, whereas the oxygen component is scarcely detected. This also indicates that nickel acetate is completely converted into metallic Ni nanocrystals during the reduction process.

The Ni nanocrystals uniformly dispersed within the carbon matrix transformed into hollow NiO nanospheres by the well-known nanoscale Kirkendall diffusion process, during which the carbon material was eliminated by combustion into carbon dioxide. The characteristics of the Kirkendall-300 nanofibers are shown in Figure 2. The overall structure of the electrospun nanofibers is well-preserved, even after the oxidation process at 400 °C, as shown in the SEM image. The TEM image shown in Figure 2c reveals the hollow nanospheres in the size range of 4−9 nm. The shell thickness of the hollow NiO nanospheres is 2 nm. The TEM image shown in Figure 2e clearly reveals the lattice fringes with an equal interplanar distance of 0.24 nm, corresponding to the (111) crystal plane of NiO crystal.

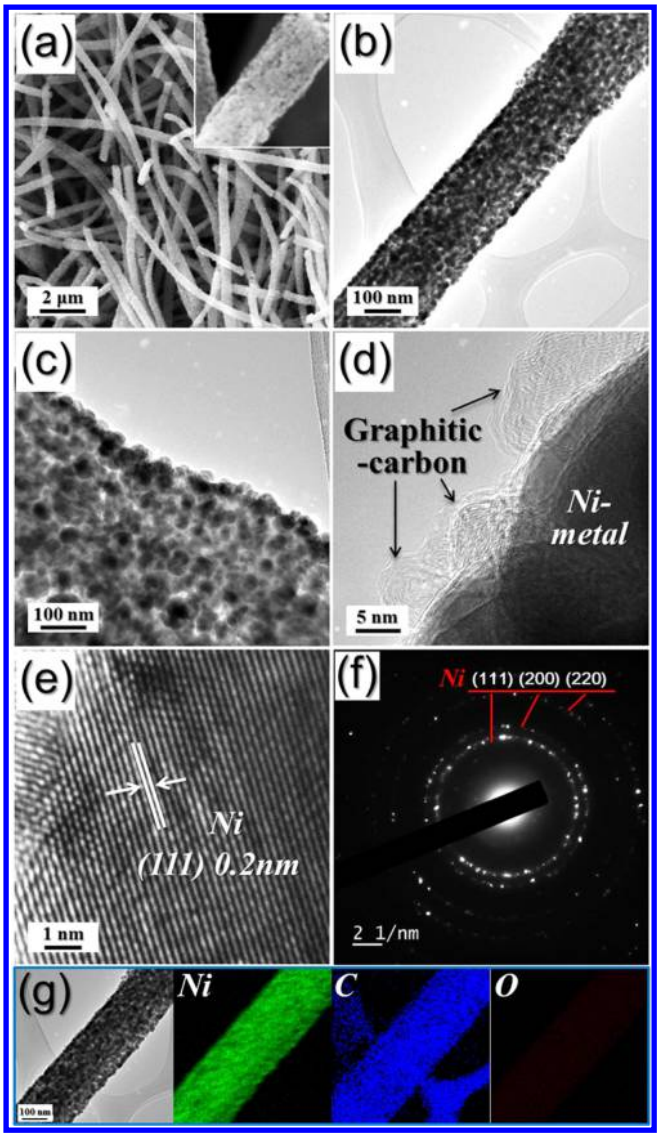

Figure 1. Morphologies, SAED pattern, and elemental mapping images of the Ni−C nanofibers: (a) SEM, (b−d) TEM images, (e) HR-TEM image, (f) SAED pattern, and (g) elemental mapping images.

The morphologies of the Kirkendall-500 nanofibers are shown in Figure 3. The Kirkendall-500 nanofibers reveal morphologies similar to those of the Kirkendall-300 nanofibers. However, the high-magnification TEM images show that the hollow nanospheres of the two nanofibers have different sizes. The hollow nanospheres in the size range of 8−15 nm are observed in the TEM images shown in Figure 3c,d. Figure 3e reveals the lattice fringes with an equal interplanar distance of 0.21 nm, corresponding to the (200) crystal plane of NiO crystal. The SAED patterns shown in Figures 2f and 3f reveal the formation of pure crystalline phase NiO nanofibers by posttreatment at 400 °C. The XRD patterns shown in Supporting Information Figure S3 also reveal that Kirkendall-300 and Kirkendall-500 are pure crystalline phase NiO nanofibers.

In contrast, the Kirkendall-700 nanofibers shown in Figure 4a,b have a rough surface due to the larger hollow nanospheres. The TEM images shown in Figure 4b,c reveal the NiO hollow nanospheres. However, the TEM image shown in Figure 4d

DOI: 10.1021/acsami.5b08793
ACS Appl. Mater. Interfaces 2015, 7, 25641−25647

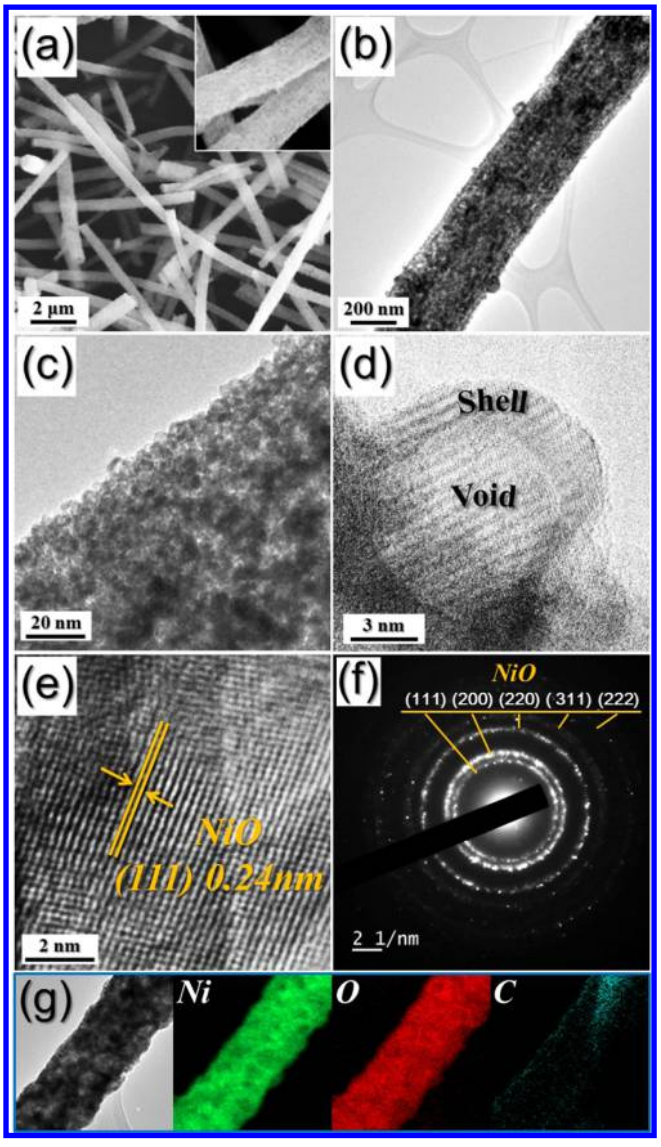

Figure 2. Morphologies, SAED pattern, and elemental mapping images of the Kirkendall-300 nanofibers: (a) SEM image, (b–d) TEM images, (e) HR-TEM image, (f) SAED pattern, and (g) elemental mapping images.

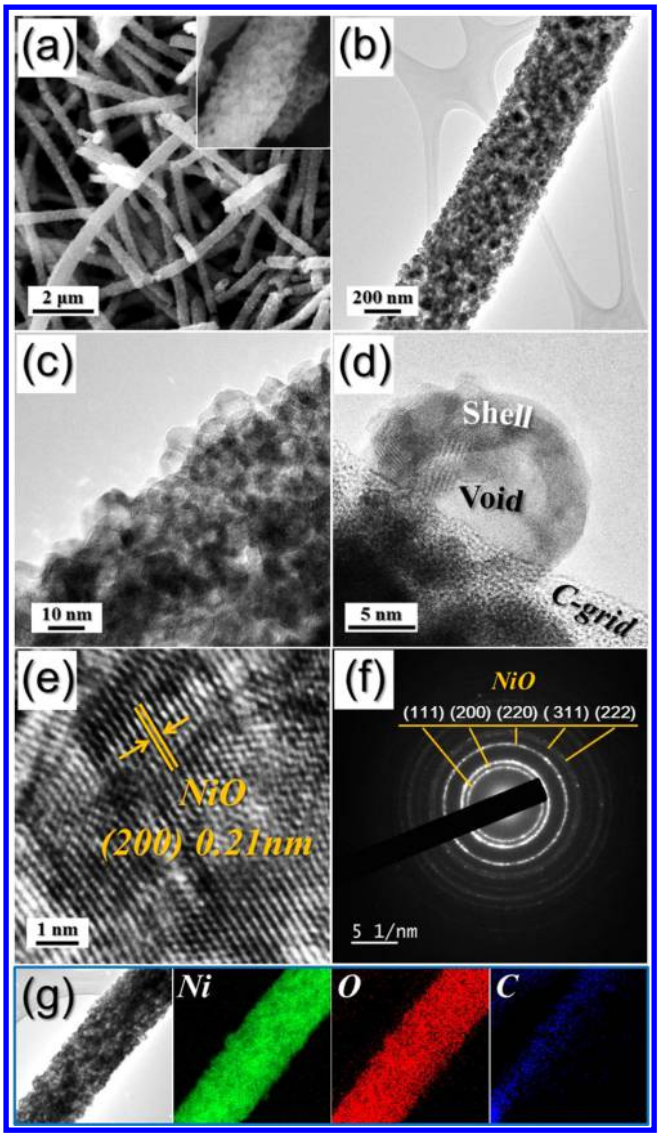

Figure 3. Morphologies, SAED pattern, and elemental mapping images of the Kirkendall-500 nanofibers: (a) SEM image, (b–d) TEM images, (e) HR-TEM image, (f) SAED pattern, and (g) elemental mapping images.

reveals the yolk–shell structure. Figure 4e clearly reveals the lattice fringes with an equal interplanar distance of 0.24 and 0.18 nm, corresponding to the (111) and (200) crystal planes of NiO and metallic Ni crystals, respectively. The SAED and XRD patterns in Figure 4f and SI Figure S3 also reveal the formation of NiO–Ni composite nanofibers from the Ni–C nanofibers reduced at 700 °C. Complete oxidation of the large Ni nanocrystals did not occur at 400 °C for 3 h. The formation mechanism of the Kirkendall-700 nanofibers composed of nanospheres with configuration of Ni@void@NiO is shown in Supporting Information Figure S4.

The formation mechanism of NiO nanofibers comprising different sized hollow nanospheres is described in Scheme 1. The size of the metal oxide hollow nanosphere is determined by the size of the metal nanopowder. In this respect, Ni–C composite nanofibers with uniformly dispersed Ni nanocrystals were prepared with various mean sizes by varying the reduction temperature of the electrospun nanofibers. The Ni–C composite nanofibers formed at a low reduction temperature followed by oxidation, resulted in nanofibers consisting of hollow NiO nanospheres of a few nanometers in size. Conversely, the Ni–C composite nanofibers formed at a high reduction temperature followed by oxidation, resulted in nanofibers consisting of hollow NiO nanospheres of several tens of nanometers in size. The detailed formation mechanism of a NiO hollow nanosphere is elucidated in Scheme 2. The posttreatment of the electrospun nanofibers under reducing atmosphere produced nickel–carbon composite nanofibers (Scheme 2, step ①). The solid Ni nanocrystals were converted into hollow NiO nanospheres during the subsequent heating process by the well-known nanoscale Kirkendall diffusion process. The void formation by Kirkendall effect was first reported by Aldinger.[37] The surface oxidation of Ni nanocrystal forms an intermediate Ni@NiO core–shell structure (Scheme 2, step ②). Ni cations with small ionic radius diffused outward more quickly than oxygen anions with large ionic radius diffused inward. Accordingly, Kirkendall voids were generated near the Ni/NiO interface (Scheme 2, step ③). Complete

DOI: 10.1021/acsami.5b08793
ACS Appl. Mater. Interfaces 2015, 7, 25641–25647

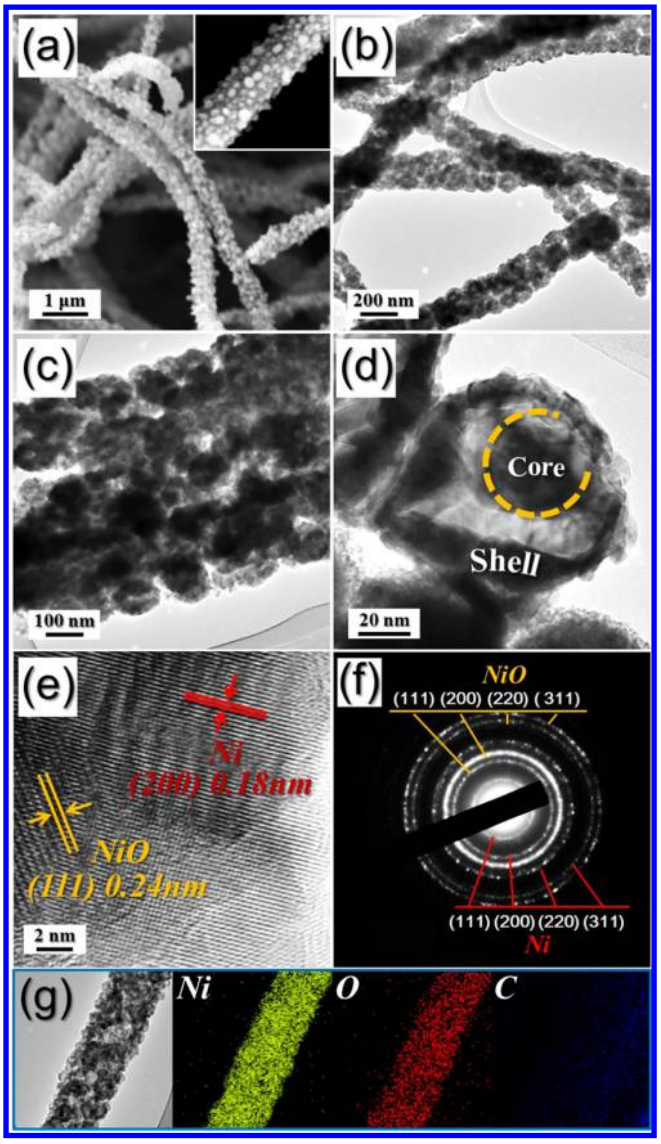

Figure 4. Morphologies, SAED pattern, and elemental mapping images of the Kirkendall-700 nanofibers: (a) SEM image, (b–d) TEM images, (e) HR-TEM image, (f) SAED pattern, and (g) elemental mapping images.

oxidation of Ni metal resulted in NiO hollow nanosphere (Scheme 2, step ④).

The XPS spectra in Supporting Information Figure S5 also indicate incomplete oxidation of the Ni nanocrystals formed at a high reducing temperature (700 °C). The XPS spectra of the Ni 2p for the samples after reduction at 300, 500, and 700 °C clearly demonstrate metallic Ni at 852.9 eV, along with NiO (Ni^{2+}, 854.5 eV) and Ni_2O_3 (Ni^{3+}, 855.8 eV). Nickel oxide was formed by surface oxidation of Ni nanocrystals. After oxidation at 400 °C, the Kirkendall-300 and Kirkendall-500 samples show only Ni peaks for the oxide, with binding energies of NiO (Ni^{2+}, 854.5 eV) and Ni_2O_3 (Ni^{3+}, 855.8 eV), as shown in SI Figure S4d,e. However, the metallic Ni peak at 852.7 eV remains for the Kirkendall-700 nanofibers. The Ni/NiO ratio in the composite nanofibers analyzed from the TOPAS program based on Rietveld refinement is 76/24. The elemental mapping images shown in Figures 2g, 3g, and 4g reveal trace amounts of carbon in the NiO nanofibers. The small amount of amorphous carbon covering the Ni nanocrystals changed into graphitic carbon during reduction. The graphitic carbon was not completely eliminated during the oxidation process conducted at 400 °C. The TGA curves in Supporting Information Figure S6 also reveal the formation of NiO nanofibers with low impurities, irrespective of the reduction temperatures. The BET surface areas of the NiO nanofibers obtained from the nanofibers reduced at 300, 500, and 700 °C are 28, 47, and 46 $m^2\ g^{-1}$, respectively. The Kirkendall-300 nanofibers with dense structure have the minimum BET surface area.

The porous NiO nanofibers shown in Supporting Information Figure S7 have over morphologies similar to those of the Kirkendall-300 and Kirkendall-500 nanofibers. However, SI Figure S7c shows the TEM image of the solid NiO nanocrystals with a mean size of 23 nm composing the porous nanofiber. The high-resolution TEM image, SAED and XRD patterns, and elemental mapping images shown in SI Figure S7 reveal the formation of pure phase NiO nanofibers by direct oxidation of electrospun nanofibers.

The electrochemical properties of the nanofibers composed of hollow NiO nanospheres are compared with those of the porous-structured NiO nanofibers in Figure 5 and Supporting Information Figures S8, S9, and S10. The CV curves obtained for the four samples are shown in SI Figure S8 for the first five cycles at a scan rate of 0.07 mV s^{-1}. A distinct reduction peak around 0.42 V is observed in the first cathodic sweep of the four samples due to the reduction of NiO to metallic Ni and the formation of amorphous Li_2O.[26,31−33] However, the reduction peak of the NiO−Ni composite nanofibers obtained from the Ni−C nanofibers reduced at 700 °C was shifted to a high-voltage range around 0.51 V, because metallic Ni in the structure provides a highly conductive medium for electron transfer.[35,36] The Kirkendall-300 and Kirkendall-500 nanofibers and the porous-structured NiO nanofibers have higher reduction peak intensities in their first cathodic sweep than that of the Kirkendal-700 nanofibers. The initial discharge curve of the NiO−Ni composite nanofibers at a current density of 1 A g^{-1} also reveals the lowest initial discharge capacity, as shown in Figure 5a. The inactivity of the Ni component in the NiO−Ni composite nanofibers results in a low lithium-ion storage property. The main reduction peak of the four samples shifts to a higher potential after the first cycle due to the formation of ultrafine nanocrystals during the first cycle. The two broad oxidation peaks, due to the oxidation of Ni to NiO and the subsequent decomposition of the SEI layer, are observed from the first cycle onward at around 1.6 and 2.3 V, respectively.[26,31−33] The good overlapping of the reduction and oxidation peaks of the nanofibers composed of hollow nanospheres from the second cycle onward reveals their good reversible lithium-ion storage performances. The initial discharge capacities of the Kirkendall-300, Kirkendall-500, and Kirkendall-700 nanofibers observed in Figure 5a are 1000, 998, and 584 mA h g^{-1}, respectively, and their corresponding initial charge capacities are 766, 729, and 381 mA h g^{-1}, respectively. The porous-structured NiO nanofibers have slightly lower initial discharge and charge capacities than those of the Kirkendall-300 and Kirkendall-500 nanofibers as shown in Figure 5a. The cycling performances of the four samples at a current density of 1 A g^{-1} are shown in Figure 5b. The nanofibers composed of hollow nanospheres have superior cycling performance compared with that of the porous-structured NiO nanofibers. The discharge capacities of the Kirkendall-300, Kirkendall-500, and Kirkendall-700 nanofibers for the 250th cycle are 707, 655, and 261 mA h g^{-1},

DOI: 10.1021/acsami.5b08793
ACS Appl. Mater. Interfaces 2015, 7, 25641−25647

Scheme 1. Formation Scheme of the NiO Nanofibers Comprised with Different Sized Hollow Nanospheres

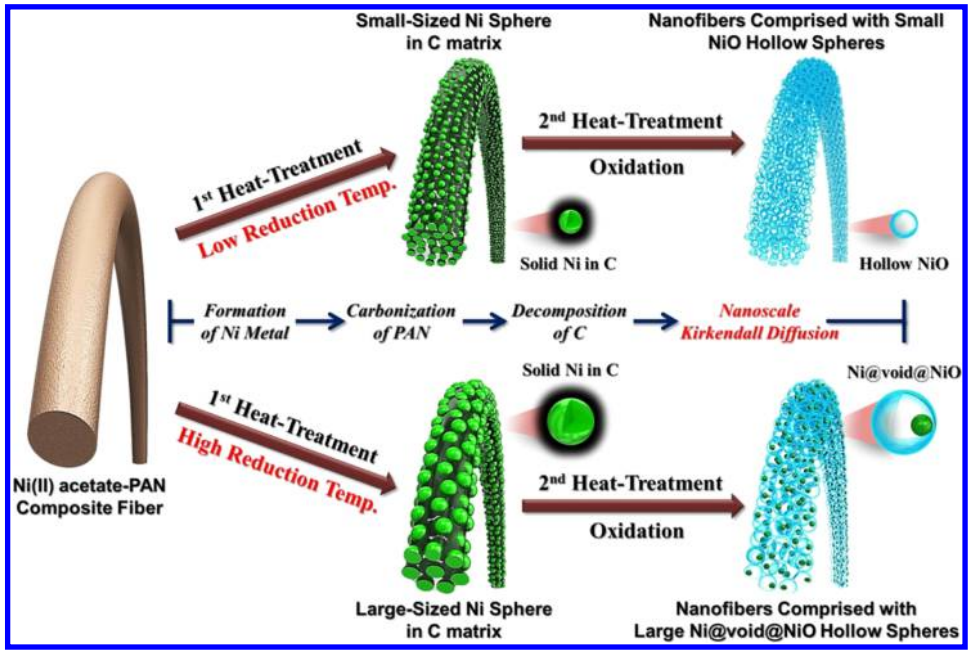

Scheme 2. Formation Mechanism of a Hollow NiO Nanosphere in the Nanofiber by Kirkendall Diffusion Effect and Its Chemical Conversion Process in the Surface Region of a Sphere

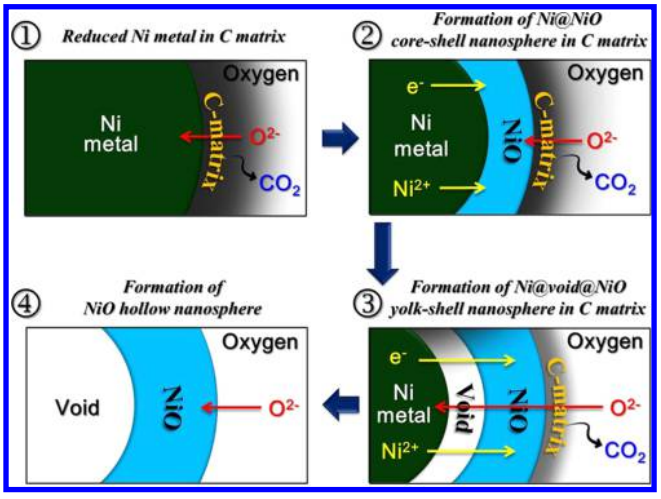

respectively. However, the discharge capacities of the porous-structured NiO nanofibers for the second and 250th cycles are 721 and 206 mA h g^{-1}, respectively. The capacity retentions of the Kirkendall-300, Kirkendall-500, and porous-structured NiO nanofibers measured from the second cycle were 96, 90, and 29%, respectively. Figure 5c shows the rate performances of the four samples with a stepwise increase in the current density from 0.1 to 3.0 A g^{-1}. The discharge capacities of the Kirkendall-500 nanofibers showing the best rate performance decrease from 787 to 636 mA h g^{-1} when the current densities increase from 0.3 to 3.0 A g^{-1}. In comparison, the discharge capacities of the porous-structured NiO nanofibers decrease from 816 to 530 mA h g^{-1} when the current densities increase from 0.3 to 3.0 A g^{-1}.

Electrochemical impedance spectroscopy measurements of the four samples were performed to explain the superior

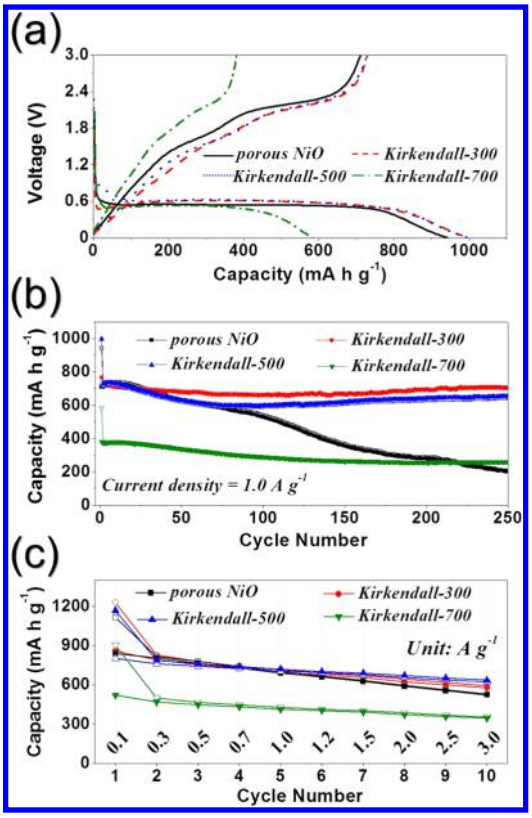

Figure 5. Electrochemical properties of the four samples: (a) initial charge/discharge curves at a constant current density of 1.0 A g^{-1}, (b) cycling performances at a constant current density of 1.0 A g^{-1}, and (c) rate performances.

lithium-ion storage properties of the nanofibers composed of hollow NiO nanospheres. The Nyquist plots display compressed semicircles in the medium-frequency range, which describe the charge-transfer resistance (R_{ct}) of the electrode.[38−40] The precise values of R_{ct} are calculated from a simulated equivalent circuit. The NiO−Ni nanofibers com-

DOI: 10.1021/acsami.5b08793
ACS Appl. Mater. Interfaces 2015, 7, 25641−25647

posed of large hollow nanospheres show the lowest R_{ct} of 82.4 Ω before cycling, as shown in SI Figure S9a. The R_{ct} of the four samples abruptly decrease after the first cycle due to the formation of ultrafine nanocrystals during the first discharge and charge processes. The R_{ct} of the nanofibers obtained by the nanoscale Kirkendall diffusion process increase slightly from 13.4 to 18.6 Ω for Kirkendall-300, from 24.4 to 33.3 Ω for Kirkendall-500, and from 20.7 to 26.8 Ω for Kirkendall-700 as the number of cycles increases from first to 100th cycle, as shown in SI Figure S9b−d. In particular, the R_{ct} of the nanofibers obtained by the nanoscale Kirkendall diffusion process for the 50th and 100th cycles are almost the same. However, the R_{ct} of the porous-structured NiO nanofibers increase steadily from 23.0 to 74.1 Ω during the 100 cycles, as shown in SI Figure S9e. The structural destruction of the porous-structured NiO nanofibers during cycling increases the charge-transfer resistances during cycling. On the other hand, the nanofibers composed of hollow nanospheres have high structural stability during rcycling due to their accommodation of large volume changes during cycling. To support this proof obviously, the morphologies of the nickel oxide nanofibers obtained after 200 cycles are shown in SI Figure S10. The nanofibers (Kirkendall-300 and Kirkendall-500) composed of hollow NiO nanospheres maintained their original morphologies well even after long-term cycling as shown by TEM images. In the case of "Kirkendall-700" composed of large spheres with mixed phases of Ni and NiO, the structure also maintained its morphologies to some degree. However, the structure of the NiO nanofiber with porous structure was not observed in the TEM images obtained after cycling.

CONCLUSIONS

In this study, metal oxide nanofibers composed of hollow nanospheres with various sizes were prepared by employing the nanoscale Kirkendall diffusion process to metal−carbon composite nanofibers. The new strategy was applied in the preparation of NiO nanofibers composed of hollow nanospheres. Changing the reduction temperature of the electrospun nanofibers produced Ni−C composite nanofibers with Ni nanocrystals of various sizes. The Ni−C composite nanofibers formed at a low reduction temperature (300 °C) resulted in NiO nanofibers consisting of hollow NiO nanospheres a few nanometers in diameter after the nanoscale Kirkendall diffusion process. However, the Ni−C composite nanofibers formed at a high reduction temperature (700 °C) resulted in NiO−Ni nanofibers consisting of yolk−shell nanospheres with diameters of several tens of nanometers after the nanoscale Kirkendall diffusion process. The NiO nanofibers with smaller hollow NiO nanospheres showed superior cycling performance for lithium-ion storage compared to that of the porous-structured NiO nanofibers formed by the same electrospinning process. The strategy introduced in this study could be applied to the preparation of metal oxide nanofibers composed of hollow nanospheres with controlled sizes for wide applications including energy storage.

ASSOCIATED CONTENT

Supporting Information

The Supporting Information is available free of charge on the ACS Publications website at DOI: 10.1021/acsami.5b08793.

Formation mechanism of a hollow NiO nanosphere, SEM, TG, and XRD pattern of as-spun $Ni(OCOCH_3)_2 \cdot 4H_2O$-PAN composite nanofibers by electrospinning process, XRD patterns of the Ni−C nanofibers, XRD patterns of the NiO nanofibers, formation mechanism of the Kirkendall-700 nanofibers, Ni 2p XPS spectra of the nanofibers reduced at 300, 500, and 700 °C and subsequently oxidized at 400 °C, TG curves of the Kirkendall-300, Kirkendall-500, Kirkendall-700, and porous-structured NiO nanofibers, characteritics of the porous-structured NiO nanofibers, cyclic voltammogram curves of the porous-structured NiO, Kirkendall-300, Kirkendall-500, and Kirkendall-700 nanofibers, Nyquist impedance plots of the Kirkendall-300, Kirkendall-500, Kirkendall-700, and porous-structured NiO nanofibers before cycling, Nyquist impedance plots of the Kirkendall-300, Kirkendall-500, Kirkendall-700, and porous-structured NiO nanofibers, fractured end image of the Kirkendall-500 nanofiber, N_2 adsorption−desorption isotherms for the Kirkendall-300, Kirkendall-500, Kirkendall-700, and porous-structured NiO nanofibers (PDF)

AUTHOR INFORMATION

Corresponding Author

*E-mail: yckang@korea.ac.kr. Fax: (+82) 2-928-3584.

Notes

The authors declare no competing financial interest.

ACKNOWLEDGMENTS

This work was supported by the Energy Efficiency & Resources Core Technology Program of the Korea Institute of Energy Technology Evaluation and Planning (KETEP) and granted financial resources from the Ministry of Trade, Industry & Energy, Republic of Korea (Grant 201320200000420).

REFERENCES

(1) Liu, J. Charging Graphene for Energy. *Nat. Nanotechnol.* **2014**, *9*, 739−741.

(2) Zhou, X.; Dai, Z.; Liu, S.; Bao, J.; Guo, Y. G. Ultra-Uniform SnO_x/Carbon Nanohybrids toward Advanced Lithium-Ion Battery Anodes. *Adv. Mater.* **2014**, *26*, 3943−3949.

(3) Chen, J.; Xu, L. N.; Li, W. Y.; Gou, X. L. α-Fe_2O_3 Nanotubes in Gas Sensor and Lithium-Ion Battery Applications. *Adv. Mater.* **2005**, *17*, 582−586.

(4) Lou, X. W.; Archer, L. A.; Yang, Z. Hollow Micro-/Nanostructures: Synthesis and Applications. *Adv. Mater.* **2008**, *20*, 3987−4019.

(5) Dong, Y.; Zhao, Z.; Wang, Z.; Liu, Y.; Wang, X.; Qiu, J. Dually Fixed SnO_2 Nanoparticles on Graphene Nanosheets by Polyaniline Coating for Superior Lithium Storage. *ACS Appl. Mater. Interfaces* **2015**, *7*, 2444−2451.

(6) Zhang, W. M.; Wu, X. L.; Hu, J. S.; Guo, Y. G.; Wan, L. J. Carbon Coated Fe_3O_4 Nanospindles as a Superior Anode Material for Lithium-Ion Batteries. *Adv. Funct. Mater.* **2008**, *18*, 3941−3946.

(7) Fan, H. J.; Gösele, U.; Zacharias, M. Formation of Nanotubes and Hollow Nanoparticles Based on Kirkendall and Diffusion Processes: A Review. *Small* **2007**, *3*, 1660−1671.

(8) Niu, C.; Meng, J.; Han, C.; Zhao, K.; Yan, M.; Mai, L. VO_2 Nanowires Assembled into Hollow Microspheres for High-Rate and Long-Life Lithium Batteries. *Nano Lett.* **2014**, *14*, 2873−2878.

(9) Wang, J.; Yang, N.; Tang, H.; Dong, Z.; Jin, Q.; Yang, M.; Kisailus, D.; Zhao, H.; Tang, Z.; Wang, D. Accurate Control of Multishelled Co_3O_4 Hollow Microspheres as High-Performance Anode Materials in Lithium-Ion Batteries. *Angew. Chem.* **2013**, *125*, 6545−6548.

DOI: 10.1021/acsami.5b08793
ACS Appl. Mater. Interfaces 2015, 7, 25641−25647

(10) Zhou, X.; Yin, Y. X.; Wan, L. J.; Guo, Y. G. A Robust Composite of SnO_2 Hollow Nanospheres Enwrapped by Graphene as a High-Capacity Anode Material for Lithium-Ion Batteries. *J. Mater. Chem.* **2012**, *22*, 17456−17459.
(11) Jana, S.; Chang, J. W.; Rioux, R. M. Synthesis and Modeling of Hollow Intermetallic Ni−Zn Nanoparticles Formed by the Kirkendall Effect. *Nano Lett.* **2013**, *13*, 3618−3625.
(12) Hong, Y. J.; Son, M. Y.; Kang, Y. C. One-Pot Facile Synthesis of Double-Shelled SnO_2 Yolk-Shell-Structured Powders by Continuous Process as Anode Materials for Li-ion Batteries. *Adv. Mater.* **2013**, *25*, 2279−2283.
(13) Cao, K.; Jiao, L.; Liu, H.; Liu, Y.; Wang, Y.; Guo, Z.; Yuan, H. 3D Hierarchical Porous α-Fe_2O_3 Nanosheets for High-Performance Lithium-Ion Batteries. *Adv. Energy Mater.* **2015**, *5*, 1401421.
(14) Cao, K.; Jiao, L.; Xu, H.; Liu, H.; Kang, H.; Zhao, Y.; Liu, Y.; Wang, Y.; Yuan, H. Reconstruction of Mini-Hollow Polyhedron Mn_2O_3 Derived from MOFs as a High-Performance Lithium Anode Material. *Adv. Sci.* **2015**, DOI: 10.1002/advs.201500185.
(15) Cho, J. S.; Hong, Y. J.; Lee, J. H.; Kang, Y. C. Design and Synthesis of Micron-Sized Spherical Aggregates Composed of Hollow Fe_2O_3 Nanospheres for Use in Lithium-Ion Batteries. *Nanoscale* **2015**, *7*, 8361−8367.
(16) Wang, D.; Yu, Y.; He, H.; Wang, J.; Zhou, W.; Abruña, H. D. Template-Free Synthesis of Hollow-Structured Co_3O_4 Nanoparticles as High-Performance Anodes for Lithium-Ion Batteries. *ACS Nano* **2015**, *9*, 1775−1781.
(17) Li, M.; Lu, Q.; Nuli, Y.; Qian, X. Core-Shell and Hollow Microspheres Composed of Tin Oxide Nanocrystals as Anode Materials for Lithium-Ion Batteries. *Electrochem. Solid-State Lett.* **2007**, *10*, K33−K37.
(18) Wang, B.; Chen, J. S.; Wu, H. B.; Wang, Z.; Lou, X. W. Quasiemulsion-Templated Formation of α-Fe_2O_3 Hollow Spheres with Enhanced Lithium Storage Properties. *J. Am. Chem. Soc.* **2011**, *133*, 17146−17148.
(19) Pervez, S. A.; Kim, D.; Farooq, U.; Yaqub, A.; Choi, J. H.; Lee, Y. J.; Doh, C. H. Comparative Electrochemical Analysis of Crystalline and Amorphous Anodized Iron Oxide Nanotube Layers as Negative Electrode for LIB. *ACS Appl. Mater. Interfaces* **2014**, *6*, 11219−11224.
(20) Li, Y.; Tan, B.; Wu, Y. Mesoporous Co_3O_4 Nanowire Arrays for Lithium Ion Batteries with High Capacity and Rate Capability. *Nano Lett.* **2008**, *8*, 265−270.
(21) Liu, S.; Wang, Z.; Yu, C.; Wu, H. B.; Wang, G.; Dong, Q.; Qiu, J.; Eychmüller, A.; Lou, X. W. D. A Flexible TiO_2(B)-Based Battery Electrode with Superior Power Rate and Ultralong Cycle Life. *Adv. Mater.* **2013**, *25*, 3462−3467.
(22) Meduri, P.; Pendyala, C.; Kumar, V.; Sumanasekera, G. U.; Sunkara, M. K. Hybrid Tin Oxide Nanowires as Stable and High Capacity Anodes for Li-Ion Batteries. *Nano Lett.* **2009**, *9*, 612−616.
(23) Teh, P. F.; Pramana, S. S.; Sharma, Y.; Ko, Y. W.; Madhavi, S. Electrospun $Zn_{1-x}Mn_xFe_2O_4$ Nanofibers as Anodes for Lithium-Ion Batteries and the Impact of Mixed Transition Metallic Oxides on Battery Performance. *ACS Appl. Mater. Interfaces* **2013**, *5*, 5461−5467.
(24) Zhang, L.; Zhao, K.; Xu, W.; Dong, Y.; Xia, R.; Liu, F.; He, L.; Wei, Q.; Yan, M.; Mai, L. Integrated SnO_2 Nanorod Array with Polypyrrole Coverage for High-Rate and Long-Life Lithium Batteries. *Phys. Chem. Chem. Phys.* **2015**, *17*, 7619−7623.
(25) Chaudhari, S.; Srinivasan, M. 1D Hollow α-Fe_2O_3 Electrospun Nanofibers as High Performance Anode Material for Lithium Ion Batteries. *J. Mater. Chem.* **2012**, *22*, 23049−23056.
(26) Wang, N.; Chen, L.; Ma, X.; Yue, J.; Niu, F.; Xu, H.; Yang, J.; Qian, Y. Facile Synthesis of Hierarchically Porous NiO Micro-Tubes as Advanced Anode Materials for Lithium-Ion Batteries. *J. Mater. Chem. A* **2014**, *2*, 16847−16850.
(27) Han, H.; Song, T.; Bae, J. Y.; Nazar, L. F.; Kim, H.; Paik, U. Nitridated TiO_2 Hollow Nanofibers as an Anode Material for High Power Lithium Ion Batteries. *Energy Environ. Sci.* **2011**, *4*, 4532−4536.
(28) Cho, J. S.; Hong, Y. J.; Kang, Y. C. Design and Synthesis of Bubble-Nanorod-Structured Fe_2O_3−Carbon Nanofibers as Advanced Anode Material for Li-Ion Batteries. *ACS Nano* **2015**, *9*, 4026−4035.
(29) Cho, J. S.; Kang, Y. C. Nanofibers Comprising Yolk-Shell Sn@void@SnO/SnO_2 and Hollow SnO/SnO_2 and SnO_2 Nanospheres via the Kirkendall Diffusion Effect and Their Electrochemical Properties. *Small* **2015**, *11*, 4673−4681.
(30) Hong, Y. J.; Yoon, J. W.; Lee, J. H.; Kang, Y. C. A New Concept for Obtaining SnO_2 Fiber-in-Tube Nanostructures with Superior Electrochemical Properties. *Chem. - Eur. J.* **2015**, *21*, 371−376.
(31) Wu, H.; Xu, M.; Wang, Y.; Zheng, G. Branched Co_3O_4/Fe_2O_3 Nanowires as High Capacity Lithium-Ion Battery Anodes. *Nano Res.* **2013**, *6*, 167−173.
(32) Varghese, B.; Reddy, M. V.; Yanwu, Z.; Lit, C. S.; Hoong, T. C.; Subba Rao, G. V.; Chowdari, B. V. R.; Wee, A. T. S.; Lim, C. T.; Sow, C. H. Fabrication of NiO Nanowall Electrodes for High Performance Lithium Ion Battery. *Chem. Mater.* **2008**, *20*, 3360−3367.
(33) Liu, H.; Wang, G.; Liu, J.; Qiao, S.; Ahn, H. Highly Ordered Mesoporous NiO Anode Material for Lithium Ion Batteries with an Excellent Electrochemical Performance. *J. Mater. Chem.* **2011**, *21*, 3046−3052.
(34) Sun, Y. K.; Lee, M. J.; Yoon, C. S.; Hassoun, J.; Amine, K.; Scrosati, B. The Role of AlF_3 Coatings in Improving Electrochemical Cycling of Li-Enriched Nickel-Manganese Oxide Electrodes for Li-Ion Batteries. *Adv. Mater.* **2012**, *24*, 1192−1196.
(35) Li, X.; Dhanabalan, A.; Wang, C. Enhanced Electrochemical Performance of Porous NiO−Ni Nanocomposite Anode for Lithium Ion Batteries. *J. Power Sources* **2011**, *196*, 9625−9630.
(36) Wen, W.; Wu, J. M.; Cao, M. H. NiO/Ni Powders with Effective Architectures as Anode Materials in Li-Ion Batteries. *J. Mater. Chem. A* **2013**, *1*, 3881−3885.
(37) Aldinger, F. Controlled Porosity by an Extreme Kirkendall Effect. *Acta Metall.* **1974**, *22*, 923−928.
(38) Wang, H.; Mao, N.; Shi, J.; Wang, Q.; Yu, W.; Wang, X. Cobalt Oxide-Carbon Nanosheet Nanoarchitecture as an Anode for High-Performance Lithium-Ion Battery. *ACS Appl. Mater. Interfaces* **2015**, *7*, 2882−2890.
(39) Lee, S. M.; Choi, S. H.; Kang, Y. C. Electrochemical Properties of Tin Oxide Flake/Reduced Graphene Oxide/Carbon Composite Powders as Anode Materials for Lithium-Ion Batteries. *Chem. - Eur. J.* **2014**, *20*, 15203−15207.
(40) Li, N.; Liu, G.; Zhen, C.; Li, F.; Zhang, L.; Cheng, H. M. Battery Performance and Photocatalytic Activity of Mesoporous Anatase TiO_2 Nanospheres/Graphene Composites by Template-Free Self-Assembly. *Adv. Funct. Mater.* **2011**, *21*, 1717−1722.

DOI: 10.1021/acsami.5b08793
ACS Appl. Mater. Interfaces 2015, 7, 25641−25647